Title
Pyroelectric energy conversion with large energy and power density in relaxor ferroelectric thin films

Journal
Nature Materials, 17(5)

ISSN
1476-1122

Authors
Pandya, Shishir
Wilbur, Joshua
Kim, Jieun
et al.

Publication Date
2018-05-01

DOI
10.1038/s41563-018-0059-8

Peer reviewed

ARTICLES
https://doi.org/10.1038/s41563-018-0059-8
nature materials

Pyroelectric energy conversion with large energy and power density in relaxor ferroelectric thin films

Shishir Pandya[1], Joshua Wilbur[2], Jieun Kim[1], Ran Gao[1], Arvind Dasgupta[1], Chris Dames[2,3] and Lane W. Martin[1,3*]

The need for efficient energy utilization is driving research into ways to harvest ubiquitous waste heat. Here, we explore pyroelectric energy conversion from low-grade thermal sources that exploits strong field- and temperature-induced polarization susceptibilities in the relaxor ferroelectric $0.68Pb(Mg_{1/3}Nb_{2/3})O_3$–$0.32PbTiO_3$. Electric-field-driven enhancement of the pyroelectric response (as large as $-550\,\mu C\,m^{-2}\,K^{-1}$) and suppression of the dielectric response (by 72%) yield substantial figures of merit for pyroelectric energy conversion. Field- and temperature-dependent pyroelectric measurements highlight the role of polarization rotation and field-induced polarization in mediating these effects. Solid-state, thin-film devices that convert low-grade heat into electrical energy are demonstrated using pyroelectric Ericsson cycles, and optimized to yield maximum energy density, power density and efficiency of $1.06\,J\,cm^{-3}$, $526\,W\,cm^{-3}$ and 19% of Carnot, respectively; the highest values reported to date and equivalent to the performance of a thermoelectric with an effective ZT ≈ 1.16 for a temperature change of 10 K. Our findings suggest that pyroelectric devices may be competitive with thermoelectric devices for low-grade thermal harvesting.

In the United States, nearly 68% of the primary energy produced each year is wasted as heat[1]. For example, it is projected that a single next-generation exascale supercomputer will consume 5–10% of the total power output from the average coal-fired power plant and turn virtually all of that energy into heat[2]. Therefore, considerable efforts are underway to harvest some of this waste heat. The majority of research in this regard has focused on thermoelectrics (materials that convert a temperature gradient into electrical energy via the Seebeck effect)[3]. For low-grade waste-heat (<100 °C) thermoelectrics are inherently limited by their low ZT, a dimensionless figure of merit (FoM) that requires high electrical and low thermal conductivity; a combination that is difficult to achieve[4]. For example, the widely studied Bi_2Te_3-based thermoelectrics have ZT ≈ 1, which corresponds to ~17% scaled efficiency (the ratio of the absolute to the Carnot efficiency) for low-grade heat scavenging[5]. Despite some commercial success with thermoelectrics, researchers continue to explore alternative technologies for waste-heat energy conversion, including approaches that take advantage of phenomena such as thermo-osmotic and -galvanic effects[6,7]. Here we demonstrate the potential of an approach based on pyroelectric materials.

Pyroelectric effect and pyroelectric energy conversion

The pyroelectric effect describes the temperature-dependent evolution of spontaneous polarization P (resulting in changes in the surface charge density of the material) and is parameterized by the pyroelectric coefficient, $\pi = \left(\frac{\partial P}{\partial T}\right)$. In contrast to the steady-state operation of thermoelectrics, pyroelectric energy conversion requires thermodynamic cycles that make use of a temporally varying thermal profile to extract electrical work from the pyroelectric. Such cycles mimic gas-phase cycles and a number of different thermal–electrical cycles for pyroelectric energy conversion have been proposed, including, for example, Stirling-like cycles with two isothermal and two isodisplacement processes[8,9], Carnot cycles with two isothermal and two adiabatic processes[10], and an adaptation of the Ericsson cycle, an Olsen cycle[11], which includes two isothermal and two isoelectric processes[11–16]. Early work in the exploration of these cycles revealed that these adapted Ericsson cycles can extract the maximum potential work from a pyroelectric out of all of the thermodynamic cycles studied to date[17]. In turn, much of the work in this field since this time has employed these adapted Ericsson cycles for pyroelectric energy conversion[12,13] and these approaches have produced maximum energy density, power density and scaled efficiency values of ~1 $J\,cm^{-3}$ (ref. [14]), ~30 $W\,cm^{-3}$ (ref. [16]) and 5.4% (ref. [15]), respectively. On the basis of these thermal–electrical cycles, researchers have also established that a high-performance pyroelectric energy conversion material should have a high π and low relative permittivity (ε_r), a trade-off parameterized by the FoM for pyroelectric energy conversion (FoM_{PEC}), which is $\pi^2/\varepsilon_0\varepsilon_r$ (ε_0 is the permittivity of free space)[18]. In turn, optimization of pyroelectric performance requires independently enhancing π and suppressing ε_r, which is difficult in conventional materials where dielectric and pyroelectric susceptibilities are generally enhanced by the same generic features (that is, proximity to phase transitions driven by chemistry, temperature, strain and so on)[19,20].

Identifying materials with large pyroelectric response

Such phase transitions are a hallmark of relaxor ferroelectrics such as $(1-x)Pb(Mg_{1/3}Nb_{2/3})O_3$–$xPbTiO_3$ (PMN–xPT) where changing the ferroelectric $PbTiO_3$ content results in a change in the lattice symmetry from rhombohedral, R ($x \leq 0.31$), to tetragonal, T ($x \geq 0.35$), via a bridging low-symmetry monoclinic, M ($0.31 < x < 0.35$), phase constituting the morphotropic phase boundary[21,22]. In proximity to the morphotropic phase boundary, different ferroelectric phases are nearly energetically degenerate, resulting in facile rotation of

[1]Materials Science and Engineering, University of California, Berkeley, Berkeley, CA, USA. [2]Mechanical Engineering, University of California, Berkeley, Berkeley, CA, USA. [3]Materials Sciences Division, Lawrence Berkeley National Laboratory, Berkeley, CA, USA. *e-mail: lwmartin@berkeley.edu

polarization under applied stimuli (that is, temperature[22], stress[23] and electric fields[24]). While electric-field-induced polarization rotation has been shown to result in giant electromechanical response[25,26], such field-coupling to pyroelectricity is poorly studied. The limited work in this regard has shown the possibility for enhancement of π under applied bias[27,28]; however, the mechanism for such effects remains unclear, with arguments ranging from the importance of a diffuse first-order-like phase transition between the ferroelectric and relaxor phases[29], to contributions from the secondary pyroelectric effect via field-induced piezoelectricity[30,31]. Understanding such electric field/temperature susceptibility of polarization in relaxor ferroelectrics is crucial to establishing these materials as promising candidates for pyroelectric energy conversion.

We report robust pyroelectric energy conversion that takes advantage of previously understudied strong field- and temperature-induced polarization susceptibilities in the relaxor ferroelectric $0.68Pb(Mg_{1/3}Nb_{2/3})O_3$–$0.32PbTiO_3$ (PMN–0.32PT). Electric-field-driven enhancement of the pyroelectric response to values as large as $-550\,\mu C\,m^{-2}K^{-1}$ and suppression of the dielectric response (by 72%) yield unprecedented FoM_{PEC}. Using field- and temperature-dependent pyroelectric measurements, the role of polarization rotation and field-induced polarization in mediating these large effects is explained. In turn, solid-state, thin-film devices that convert waste heat into electrical energy are demonstrated using pyroelectric Ericsson cycles yielding energy density, power density and scaled efficiency of $1.06\,J\,cm^{-3}$, $526\,W\,cm^{-3}$ and 19%, respectively; the highest values reported to date and equivalent to the performance of a thermoelectric with an effective $ZT \approx 1.16$ for $\Delta T = 10\,K$.

Probing pyroelectricity in relaxor ferroelectric thin films

We focus on 150 nm PMN–0.32PT/20 nm $Ba_{0.5}Sr_{0.5}RuO_3/NdScO_3$ (110) heterostructures grown via pulsed-laser deposition (Methods). X-ray diffraction line scans (Supplementary Fig. 1a) and reciprocal space maps (Supplementary Fig. 1b) reveal that the heterostructures are epitaxial with (001)-orientation, single-phase and coherently strained (compressive strain of −0.5%) (Methods). Pyroelectric devices were fabricated using established approaches (Methods)[32]. Briefly, these devices enable simultaneous direct measurement of dielectric, ferroelectric and pyroelectric responses and implementation of solid-state electro-thermal cycles such as pyroelectric Ericsson cycles. The technique utilizes a microfabricated heater/sensor line that localizes high-frequency periodic heating to the ferroelectric under test, allowing simultaneous direct measurements of both pyroelectric currents and temperature change and thus providing a direct quantification of π in symmetric capacitor structures in epitaxial thin films (Fig. 1a). Polarization–electric field hysteresis loops, measured from such devices, reveal high polarizability and behaviour characteristic of relaxor ferroelectrics[33] (Fig. 1b). Additional features of relaxor behaviour are evident in temperature-dependent ε_r that shows frequency dispersion below its maximum ($T_{max} = 150\,°C$) (Supplementary Fig. 2a) and deviation from Curie–Weiss behaviour below the Burns temperature ($T_b = 259\,°C$, above which the short-range-ordered domains or polar nano-regions dissolve and PMN–0.32PT is a nonpolar paraelectric)[34] (Supplementary Fig. 2b).

Pyroelectric measurements were conducted by periodically oscillating the temperature of the heterostructure by applying a sinusoidal heating current of 19 mA (r.m.s.) at a frequency of 1 kHz on the microfabricated heater line (Fig. 1a and Methods). This heating current perturbs the temperature of the heterostructure by an amplitude $\theta_{FE} = 10\,K$ at a frequency of 2 kHz and is measured using the 3ω method (Methods and Supplementary Fig. 3)[32]. The resulting pyroelectric current (i_p) was measured as a function of d.c. electric field (Fig. 1c) and π is extracted from the relationship $i_P \left(A\frac{dT}{dt}\right)^{-1}$ (red data, Fig. 1d). Under zero bias, $\pi \approx -100\,\mu C\,m^{-2}K^{-1}$; however, under application of a d.c. electric field, i_p (Fig. 1c) and π (Fig. 1d) are found to be dramatically enhanced such that $|\pi| > 550\,\mu C\,m^{-2}K^{-1}$, far surpassing the field-induced enhancement of π in a classic ferroelectric (for example, data for a (001)-oriented $PbZr_{0.2}Ti_{0.8}O_3$ thin film are provided for comparison; blue curve, Fig. 1d). We further measured the tunability of ε_r with d.c. electric field and found that ε_r is dramatically suppressed (by ~72%) with field (red open circles, Fig. 1e) due to the suppression of the extrinsic polarization contribution from the presence of polar nano-regions and consistent with prior observations in relaxor ferroelectrics[35]. In addition, the loss tangent due to charge leakage within the capacitor is also suppressed with increasing d.c. electric field (red filled squares, Fig. 1e). From a practical standpoint, strongly suppressed ε_r (and loss tangent) in conjunction with significantly enhanced π results in an enhancement of the FoM_{PEC} (red data, Fig. 1f) by ~5 times in comparison to commonly used materials (for example, $LiNbO_3$ (ref. [20]) (black data, Fig. 1f) and $PbZr_{0.2}Ti_{0.8}O_3$ (ref. [32]) (blue data, Fig. 1f)). The question, then, is: what is the role of the d.c. electric field in enhancing π to such an extent?

Exploring electric field enhancement of pyroelectricity

To probe the effect of electric field on this strongly field- and temperature-coupled relaxor ferroelectric, a series of field- and temperature-dependent pyroelectric measurements were conducted (Methods). For all studies, the heterostructures were first heated to above the T_b to 300 °C before being cooled to room temperature in zero applied field. Once at room temperature, pyroelectric measurements were conducted as a function of d.c. electric field (0, 13.3, 26.7 and $40\,kV\,cm^{-1}$) with increasing sample temperature using an oscillating a.c. temperature with amplitude $\theta_{FE} = 2.5\,K$. The magnitude of oscillation was deliberately chosen to be small to capture any temperature-dependent changes in the pyroelectric susceptibility as the background temperature was varied. Under zero field, two distinct anomalies in π are observed (Fig. 2a). We attribute the first anomaly at 82 °C to a M (specifically M_C wherein the polarization is confined to the {010}) to T phase transition[36]. The second anomaly at 216 °C probably corresponds to a T to cubic phase transition. Single-crystal PMN–0.32PT shows such a transition at <150 °C (ref. [36]); however, in the compressively strained (−0.5%) films used here, the transition temperature could easily be shifted higher. For brevity and because we are primarily interested in the room-temperature enhancement of π, we focus further analysis on the 25–120 °C window (through the M_C to T phase transition; the full temperature range from 25 to 250 °C is provided as well; Supplementary Fig. 4a). Upon probing the same pyroelectric response for heterostructures under applied d.c. electric fields of 13.3, 26.7 and $40\,kV\,cm^{-1}$, we observe field-induced enhancement of π at all temperatures (Fig. 2b). The first anomaly in π, corresponding to the M_C to T phase transition, progressively shifts to lower temperatures (as extracted from the derivative of the temperature-dependent data; Supplementary Fig. 4b) with increasing field, indicating a field-induced rotation of polarization[24,37] that could contribute to the enhancement of π. At the same time, since the same electric field can also enhance the average magnitude of the polarization of the material either by aligning the polarization within the domains or re-alignment/growth of the domains[38,39], the question arises as to whether the enhancement of π comes primarily from field-induced polarization rotation, field-induced enhancement of the average polarization or a combination thereof?

Separating induced-polarization and rotation contributions

To separate these effects, π was measured while heating under a d.c. electric field of $40\,kV\,cm^{-1}$ (field heating, FH) through the M_C to T phase transition to 125 °C (red data, Fig. 2c) and on cooling to room temperature under application of the same field (field cooling, FC) (blue data, Fig. 2c). In this situation, the transition back to the M_C phase is quenched by the applied electric field and the

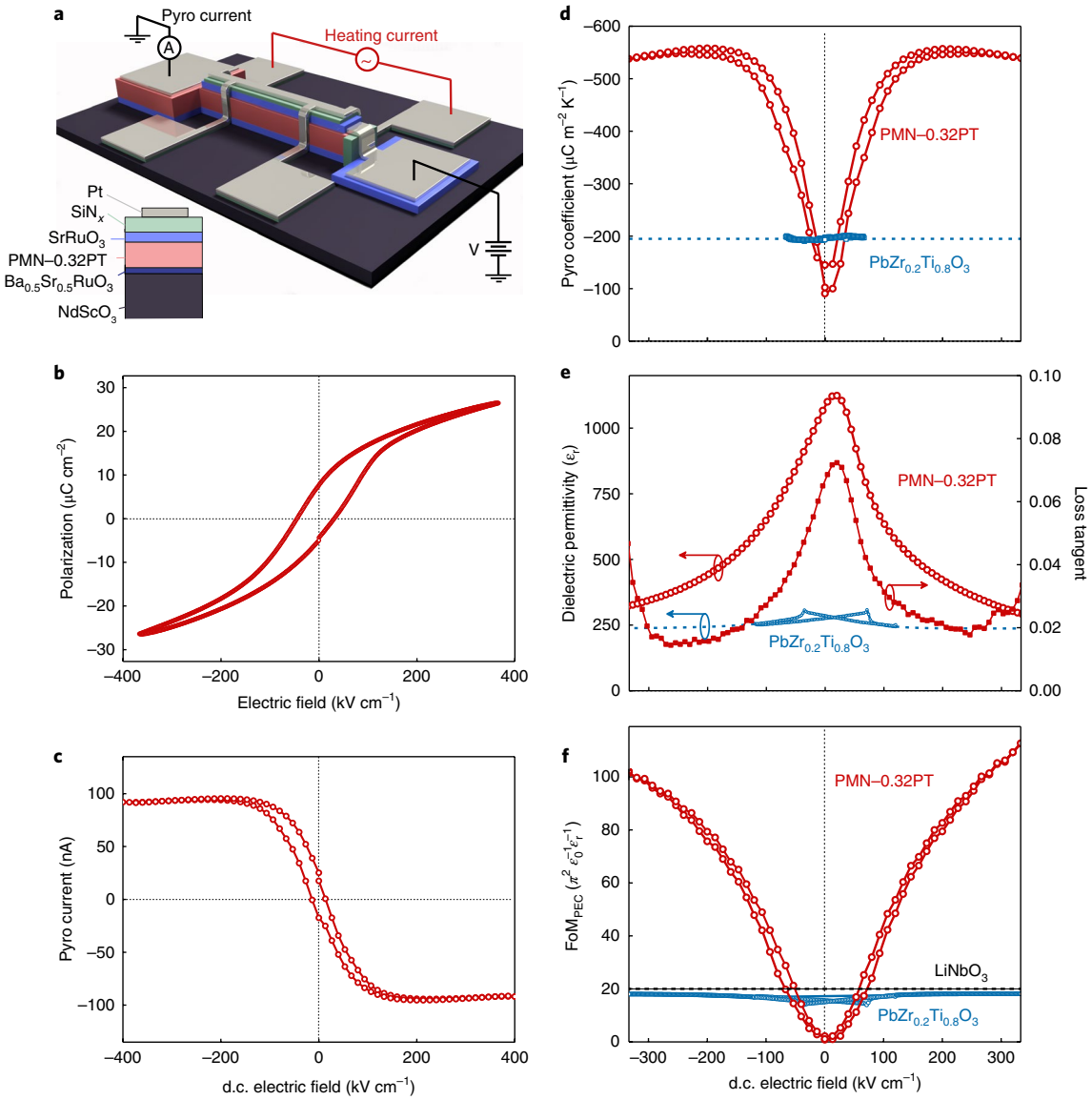

Fig. 1 | Pyroelectric and dielectric permittivity measurements of PMN–0.32PT thin films. a, A schematic illustration of the device structure wherein sinusoidally varying current applied across the microfabricated heater line locally heats the relaxor ferroelectric heterostructure resulting in pyroelectric current collected via the bottom electrode of the device while keeping the top electrode at any desired d.c. bias field. **b**, The polarization–electric field hysteresis loop measured at room temperature and 2 kHz for a PMN–0.32PT heterostructure in the device structure shown in **a**. **c**, The measured pyroelectric current (r.m.s.) for a sinusoidal oscillation of temperature with amplitude $\theta_{FE}=10$ K at 2 kHz as a function of d.c. electric field. **d**, The extracted pyroelectric coefficient $\pi = i_P\left(A\frac{dT}{dt}\right)^{-1}$ plotted as a function of d.c. electric field. **e**, The variation of ε_r (open red circles) and loss tangent (filled red squares) with applied d.c. electric field. The blue data in **d** and **e** show results for a $PbZr_{0.2}Ti_{0.8}O_3$ thin film measured in the same configuration. **f**, FoM_{PEC} as a function of applied d.c. electric field. The measured FoM_{PEC} for a $PbZr_{0.2}Ti_{0.8}O_3$ thin film (blue) and literature values for $LiNbO_3$ (black dashed line) are provided for comparison.

sample remains in the T phase (in effect, contributions to π from polarization rotation would be 'turned off'). To confirm that it is indeed 'locked' in the T phase, π was measured again while heating (FH) after the initial FH and FC cycle and, in this case, the M_C to T phase transition is not observed, confirming that the sample remained in the T phase (Supplementary Fig. 5). By comparing the difference between the FH (red) and FC (blue) curves, the contribution to π due to polarization rotation (orange data, Fig. 2c) can be quantified at any temperature. For example, polarization rotation contributes a maximum of ~16% of the total π near the phase transition. Repeating the same experiment at a higher d.c. electric field (67 kV cm^{-1}) yielded the same fractional contribution from polarization rotation (Supplementary Fig. 6). In turn, this implies that the majority of the large response under bias arises from field-induced enhancement of the average polarization. Ultimately, the combined temperature- and field-induced changes in polarization magnitude and direction yield large pyroelectric response that makes this material promising for pyroelectric energy conversion.

Solid-state pyroelectric energy conversion in thin films

Having understood the mechanism behind the large electric-field enhancement of π, we proceed to demonstrate the potential of directly converting heat into electrical energy via pyroelectric Ericsson (or Olsen) cycles. The ideal cycle begins with an isothermal (T_{low}) change of electric field ($E_{low} \rightarrow E_{high}$; $1 \rightarrow 2$, Fig. 3a) that polarizes the system. This is followed by an isoelectric (E_{high})

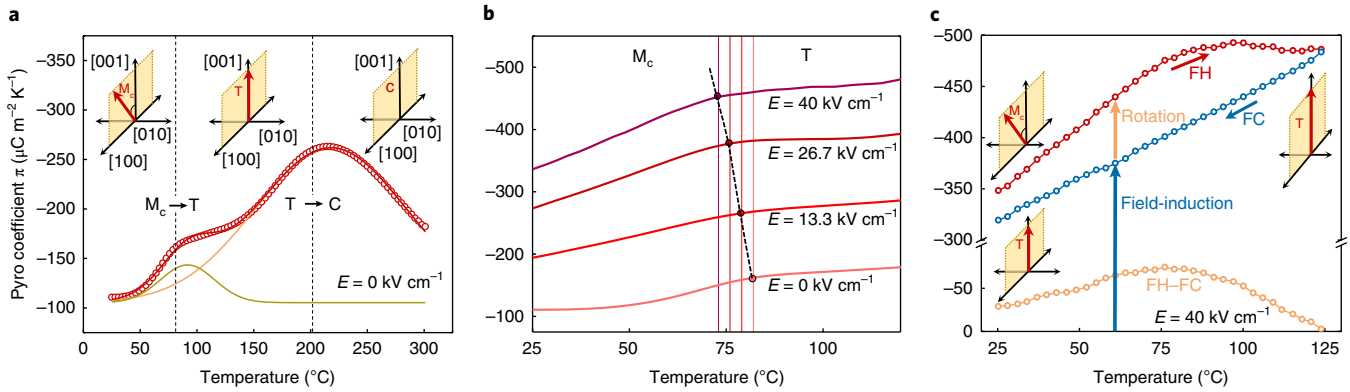

Fig. 2 | Temperature- and field-dependent pyroelectric measurements. a, Pyroelectric measurements conducted under zero-field with an oscillating a.c. temperature with amplitude $\theta_{FE} = 2.5$ K as a function of background temperature. **b**, Pyroelectric measurements under applied d.c. electric fields with dashed lines showing the transition temperature for various d.c. fields. **c**, Pyroelectric measurements under field-heating (FH, red) and -cooling (FC, blue). The difference between the FH and FC (orange) provides a quantitative measurement of the contribution of polarization rotation to the net pyroelectric susceptibility.

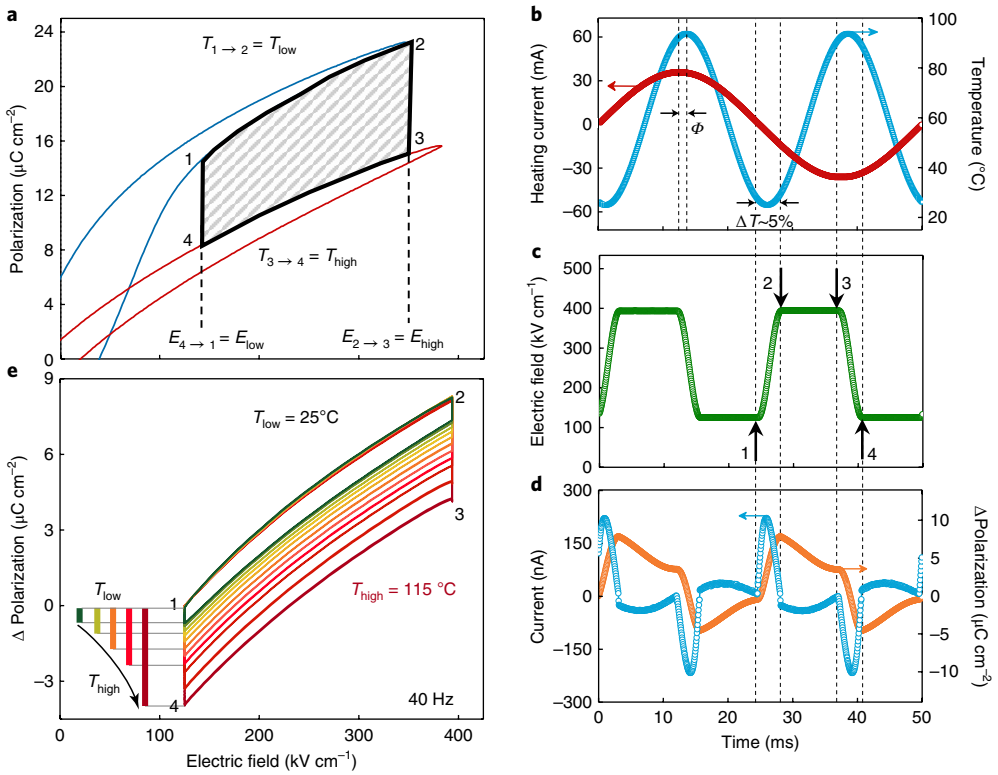

Fig. 3 | Implementation of solid-state pyroelectric Ericsson cycles for energy conversion. a, A schematic of the pyroelectric Ericsson cycle showing the various isothermal and isoelectric processes. The total energy density per cycle is given by the area of the closed loop, $\oint E \cdot dP$ (shaded region). **b**, Example of the implementation of the Ericsson cycles wherein the temperature of the heterostructure is sinusoidally varied by $\Delta T = 70$ K (blue curve) at 40 Hz by applying a sinusoidally varying current (red curve) at 20 Hz that locally heats the heterostructure via Joule heating. **c**, A periodic electric field $E(t)$, phase-synced (delayed by ϕ) with the heating current, is applied across the relaxor ferroelectric to complete the cycle. **d**, In response to the periodically varying temperature and electric field, the resulting current (blue curve) is measured and the change in polarization is calculated by integrating the current (orange curve). **e**, Experimentally obtained changes in polarization as a function of electric field for $\Delta T = 10$–90 K while keeping $T_{low} = 25$ °C with $\Delta E = 267$ kV cm^{-1} at $f = 40$ Hz.

absorption of heat ($T_{low} \rightarrow T_{high}$; 2 → 3, Fig. 3a). Next, the electric field is isothermally (T_{high}) reduced ($E_{high} \rightarrow E_{low}$; 3 → 4, Fig. 3a). Finally, the heat is expelled isoelectrically (E_{low}) ($T_{high} \rightarrow T_{low}$; 4 → 1, Fig. 3a). In our devices, this cycle is implemented by applying carefully chosen time-dependent, spatially uniform temperatures and electric fields to the relaxor ferroelectric. Akin to the pyroelectric measurements above, applying a sinusoidally varying current at 1ω that locally heats the heterostructure via Joule heating (red curve, Fig. 3b) results in the temperature of the heterostructure varying sinusoidally at 2ω with an amplitude that depends on the magnitude of the heating current (for example, $\Delta T = 70$ K; blue curve, Fig. 3b). A synchronized periodic electric field $E(t)$ is applied across

the heterostructure in a nearly square-wave fashion (Fig. 3c). In our devices, isothermal polarization and depolarization is achieved by switching the electric field exactly where the temperature achieves its extrema, thereby approximating steps 1→2 and 3→4 of the ideal Ericsson cycle (Fig. 3a). In other words, the electric field changes from high to low or vice versa while the temperature goes through a maximum or a minimum with less than 5% change in the temperature. This small, but finite, 5% temperature-change window was chosen so as not to change the electric field using a step function that results in a very large capacitive current saturating our current-to-voltage amplifier. In response to the periodically varying temperature and electric field, the resulting current shows two features, respectively: a background pyroelectric current; and dielectric current spikes (blue curve, Fig. 3d). The total current can then be integrated (Methods) to extract the change in polarization $\Delta P(t)$ (orange curve, Fig. 3d). Using this approach, plots of $\Delta P(t)$ versus $E(t)$ yield a familiar representation of the pyroelectric Ericsson cycle such as, for example, how the response changes for various magnitudes of $\Delta T = 10$–$90\,K$ (maintaining $T_{low} = 25\,°C$, $\Delta E = 267\,kV\,cm^{-1}$, and cycle frequency $f = 40\,Hz$; Fig. 3e). Data at higher cycling frequencies are also provided (Supplementary Fig. 7). Examination of these data reveals that on increasing the magnitude of ΔT, the area of the cycle in P–E space increases as more heat is converted into electrical work ($\oint E \cdot dP$).

Thin-film versus bulk pyroelectric materials

The thin-film geometry of our devices also enables application of both larger electric fields and faster temperature oscillations as compared to bulk ceramics or single crystals, allowing us to explore the pyroelectric energy conversion potential across a range of experimental conditions ($\Delta T = 10$–$110\,K$, $\Delta E = 33$–$400\,kV\,cm^{-1}$, and cycle frequency $f = 10$–$2{,}000\,Hz$). Following an initial optimization within these parameter ranges, the PMN–0.32PT thin films are shown to provide record-breaking pyroelectric energy conversion, including: first, the largest energy density of $1.06\,J\,cm^{-3}$ (at $\Delta T = 90\,K$, $\Delta E = 267\,kV\,cm^{-1}$ and $f = 40\,Hz$; Fig. 4a), which is made possible because of the large field-induced value of π and the ability to apply large electric fields maximizing the electrical work ($\oint E \cdot dP$). Second, the largest power density of $526\,W cm^{-3}$ (at $\Delta T = 56\,K$, $\Delta E = 267\,kV\,cm^{-1}$ and $f = 1{,}000\,Hz$; Fig. 4b) that is realized because the power density scales directly with cycling frequency, which can be increased because the thermal time constant of the thin-film geometry is small. Third, the largest scaled efficiency of 19%

$$\left(\frac{T_{high}}{\Delta T}\frac{\oint E \cdot dP}{\int_{T_{low}}^{T_{high}} C(T)dT}\right)$$

where $\left(\frac{T_{high}}{\Delta T}\right)^{-1}$ is the Carnot efficiency, $\oint E \cdot dP$ is the net work done and $\int_{T_{low}}^{T_{high}} C(T)dT$ is the calculated heat input to the active material with a temperature-dependent volumetric heat capacity $C(T)$[40] (at $\Delta T = 10\,K$, $\Delta E = 267\,kVcm^{-1}$ and $f = 40\,Hz$; Fig. 4c), a significant improvement over the highest reported value of ~5.4% for the same ΔT (ref. [15]). It should be noted that for the current work, $C(T)$ is assumed to change only with temperature[41,42] and is assumed to be constant with electric field[43] over the range studied herein.

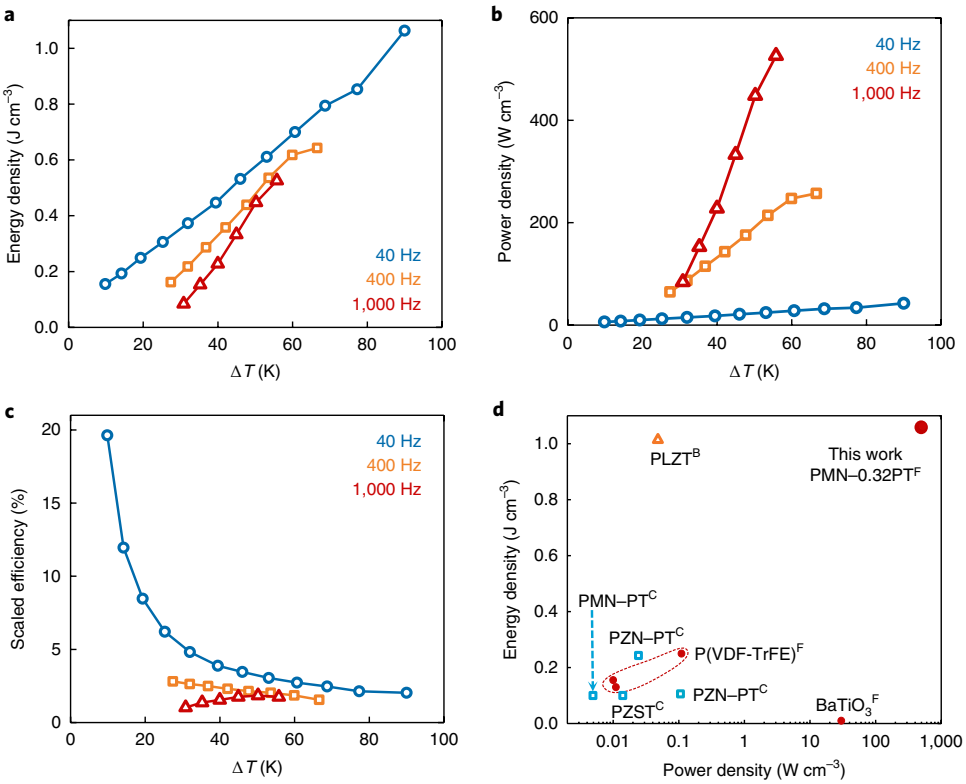

Fig. 4 | Exploring pyroelectric Ericsson cycles for energy conversion. a–c, Energy density (**a**), power density (**b**) and scaled efficiency (**c**) extracted from various pyroelectric Ericsson cycles as a function of cycle frequency (40 Hz (blue), 400 Hz (orange) and 1 kHz (red)) and ΔT while keeping $T_{low} = 25\,°C$ with $\Delta E = 267\,kV\,cm^{-1}$. **d**, Comparison of the current work with experimentally achieved energy and power densities from a number of prior studies of pyroelectric energy conversion using thermodynamic cycles. The superscripts B, C and F correspond to bulk-ceramic, single-crystal and thin-film samples, respectively.

For comparison, the energy outputs from the current work are compared to a number of experimentally investigated energy and power densities extracted from previous studies of pyroelectric energy conversion (Fig. 4d). These works employed a variety of thermal cycling methods, from pumping hot/cold fluids to immersing the pyroelectric material alternately in hot and cold thermal baths, to study bulk-ceramic ($Pb_{1-x}La_x(Zr_{0.65}Ti_{0.35})_{1-x/4}O_3$ (ref. [14])), single-crystal ($Pb_{0.99}Nb_{0.02}(Zr_{0.68}Sn_{0.25}Ti_{0.07})_{0.98}O_3$ (ref. [17]), $Pb(Zn_{1/3}Nb_{2/3})_{0.955}Ti_{0.045}O_3$ (refs [44,45]) and $Pb(Mg_{1/3}Nb_{2/3})_{0.68}Ti_{0.32}O_3$ (ref. [46])) and thin-film (P(VDF-TrFE) (refs [47–49]) and $BaTiO_3$ (ref. [16])) samples. As compared to the current work, the ultimate performance of these prior studies was limited by aspects related to the materials themselves (that is, they had intrinsically low pyroelectric coefficients) and/or to the functional form of the material (that is, inability to apply large electric fields and slow thermal cycling). In the current work, we have created a field-tuned, intrinsically large pyroelectric coefficient in conjunction with a thin-film device geometry. This thin-film geometry allows a number of important advantages over work in bulk materials, including: significantly larger sweeps of electric field (achieved with much lower voltage (V) in comparison to bulk materials), thus maximizing field-induced polarization changes and work; high-frequency, high-temperature-amplitude cycling to increase power and work, respectively; and significantly less heat input (Q_{in}) is required to increase the temperature of the lattice (since it scales with volume ($\mathbb{V}$) as $Q_{in}=\mathbb{V}\int_{T_{low}}^{T_{high}}C(T)\mathrm{d}T$) while still driving the same changes in the surface charge density with the applied voltage (V), which is equivalent to the electrical work done (which scales with area ($\mathbb{A}$) as $W=\mathbb{V}\oint E\cdot \mathrm{d}P=\mathbb{A}\oint V\cdot \mathrm{d}P$ since electric field is simply due to the applied voltage). Thus, said another way, the advantage of performing pyroelectric energy conversion with thin films is that the effects scale with just the area of the device, not the volume. Ultimately, this places pyroelectric thin films (here corresponding to an effective ZT = 1.16) as a very promising candidate for low-quality waste-heat energy harvesting, on par with thermoelectrics.

Conclusions

Large $|\pi| > 550\,\mu C\,m^{-2}\,K^{-1}$ under an application of d.c. electric field is obtained in PMN–0.32PT thin films owing to a strong field-induced enhancement of the average polarization and polarization rotation. The same electric field also suppresses ε_r by >70%, which, in turn, enhances the FoM_{PEC} by ~5 times in comparison to zero-field values and standard pyroelectric materials. Ultimately, implementation of solid-state pyroelectric Ericsson cycles yields a maximum energy density, power density and scaled efficiency of $1.06\,J\,cm^{-3}$ per cycle, $526\,W\,cm^{-3}$ per cycle and 19%, respectively; these are the highest values reported to date for pyroelectrics. The implications of this work are multi-fold. First, these results suggest that there could be novel routes to enhance the pyroelectric response in materials. Much as field-induced polarization enhancement and rotation were used herein to augment the response, other field-induced routes to large effects should also be considered (for example, field-induced domain and phase structure evolution, field-induced defect reorientation and motion and so on). This could, in turn, greatly expand the number of candidate materials for pyroelectric energy conversion. Second, this work reveals the importance of expanding the study of pyroelectric energy conversion in thin-film versions of materials since this process scales inherently with material area, not volume. At the same time, thin films permit operation at both high electric fields and thermal oscillation frequencies that can further enhance energy and power outputs. Finally, this work suggests that pyroelectric energy conversion can potentially compete with thermoelectrics, in particular, for energy harvesting from low-grade waste heat.

Methods

Methods, including statements of data availability and any associated accession codes and references, are available at https://doi.org/10.1038/s41563-018-0059-8.

Received: 15 September 2017; Accepted: 14 March 2018;
Published online: 16 April 2018

References

1. *Estimated U.S. Energy Consumption in 2016* (Livermore Lawrence National Laboratory and Department of Energy, 2017).
2. Ball, P. Computer engineering: Feeling the heat. *Nature* **492**, 174–176 (2012).
3. Bell, L. E. Cooling, heating, generating power, and recovering waste heat with thermoelectric systems. *Science* **321**, 1457–1461 (2008).
4. Vining, C. B. An inconvenient truth about thermoelectrics. *Nat. Mater.* **8**, 83–85 (2009).
5. Tritt, T. M. *Recent Trends in Thermoelectric Materials, Semiconductors and Semimetals.* Part Two (Academic Press, San Diego, 2000).
6. Straub, A. P., Yip, N. Y., Lin, S., Lee, J. & Elimelech, M. Harvesting low-grade heat energy using thermo-osmotic vapour transport through nanoporous membranes. *Nat. Energy.* **1**, 16090 (2016).
7. Lee, S. W. et al. An electrochemical system for efficiently harvesting low-grade heat energy. *Nat. Commun.* **5**, 3942 (2014).
8. Childress, J. D. Application of a ferroelectric material in an energy conversion device. *J. Appl. Phys.* **33**, 1793–1798 (1962).
9. Clingman, W. H. & Moore, R. G. Application of ferroelectricity to energy conversion processes. *J. Appl. Phys.* **32**, 675–681 (1961).
10. Drummond, J. E. Dielectric power conversion. in *Proc. 10th Annual Intersociety Energy Conversion and Engineering Conference,* 569–575 (IEEE, New York, 1975).
11. Olsen, R. B. Ferroelectric conversion of heat to electrical energy - a demonstration. *J. Energy* **6**, 91–95 (1982).
12. McKinley, I. M., Kandilian, R. & Pilon, L. Waste heat energy harvesting using the Olsen cycle on $0.945Pb(Zn_{1/3}Nb_{2/3})O_3$–$0.055PbTiO_3$ single crystals. *Smart Mater. Struct.* **21**, 035015 (2012).
13. Navid, A. & Pilon, L. Pyroelectric energy harvesting using Olsen cycles in purified and porous poly(vinylidene fluoride-trifluoroethylene) [P(VDF-TrFE)] thin films. *Smart Mater. Struct.* **20**, 025012 (2011).
14. Lee, F. Y., Jo, H. R., Lynch, C. S. & Pilon, L. Pyroelectric energy conversion using PLZT ceramics and the ferroelectric-ergodic relaxor phase transition. *Smart Mater. Struct.* **22**, 025038 (2013).
15. Sebald, G., Pruvost, S. & Guyomar, D. Energy harvesting based on Ericsson pyroelectric cycles in a relaxor ferroelectric ceramic. *Smart Mater. Struct.* **17**, 015012 (2007).
16. Bhatia, B. et al. High power density pyroelectric energy conversion in nanometer-thick $BaTiO_3$ films. *Nanoscale Microsc. Thermophys. Eng.* **20**, 137–146 (2016).
17. Olsen, R. B., Bruno, D. A. & Briscoe, J. M. Pyroelectric conversion cycles. *J. Appl. Phys.* **58**, 4709–4716 (1985).
18. Sebald, G. et al. Electrocaloric and pyroelectric properties of $0.75Pb(Mg_{1/3}Nb_{2/3})O_3$–$0.25PbTiO_3$ single crystals. *J. Appl. Phys.* **100**, 124112 (2006).
19. Karthik, J. & Martin, L. W. Pyroelectric properties of polydomain epitaxial $Pb(Zr_{1-x},Ti_x)O_3$ thin films. *Phys. Rev. B* **84**, 024102 (2011).
20. Mangalam, R. V. K., Agar, J. C., Damodaran, A. R., Karthik, J. & Martin, L. W. Improved pyroelectric figures of merit in compositionally graded $PbZr_{1-x}Ti_xO_3$ thin films. *ACS Appl. Mater. Interfaces* **5**, 13235–13241 (2013).
21. Choi, S. W., Shrout, T. R., Jang, S. J. & Bhalla, A. S. Morphotropic phase boundary in Pb $(Mg_{1/3}Nb_{2/3})O_3$–$PbTiO_3$ system. *Mater. Lett.* **8**, 253–255 (1989).
22. Noheda, B., Cox, D. E., Shirane, G., Gao, J. & Ye, Z.-J. Phase diagram of the ferroelectric relaxor $(1-x)PbMg_{1/3}Nb_{2/3}O_{3-x}PbTiO_3$. *Phys. Rev. B* **66**, 054104 (2002).
23. McLaughlin, E. A., Liu, T. & Lynch, C. S. Relaxor ferroelectric PMN–32%PT crystals under stress and electric field loading: I-32 mode measurements. *Acta Mater.* **52**, 3849–3857 (2004).
24. Davis, M., Damjanovic, D. & Setter, N. Electric-field-, temperature-, and stress-induced phase transitions in relaxor ferroelectric single crystals. *Phys. Rev. B* **73**, 1–16 (2006).
25. Fu, H. & Cohen, R. Polarization rotation mechanism for ultrahigh electromechanical response in single-crystal piezoelectrics. *Nature* **403**, 281–283 (2000).
26. Kutnjak, Z., Petzelt, J. & Blinc, R. The giant electromechanical response in ferroelectric relaxors as a critical phenomenon. *Nature* **441**, 956–959 (2006).
27. Kim, Y. J., Choi, S. W. & Bhalla, A. S. Dielectric, pyroelectric properties, and morphotropic phase boundary in La-doped $(1-x)Pb(Mg_{1/3}Ta_{2/3})$–$xPbTiO_3$ solid solution ceramics. *Ferroelectrics* **173**, 87–96 (1995).
28. Taylor, D. J., Damjanovic, D. & Bhalla, A. S. Pyroelectric and dielectric properties of pmn-based ceramics under dc bias. *Ferroelectrics* **118**, 143–155 (1991).
29. Raevskaya, S. I. et al. Critical nature of the giant field-induced pyroelectric response in single crystals. *Appl. Phys. Lett.* **93**, 042903 (2008).

30. Smirnova, E. P. & Sotnikov, A. V. Pyroelectric and elastic properties of lead magnesium niobate- and barium titanate-based solid solutions near a phase transition. *Phys. Solid State* **48**, 102–105 (2006).
31. Smirnova, E. P., Aleksandrov, S. E., Sotnikov, K. A., Kapralov, A. A. & Sotnikov, A. V. Pyroelectric effect in lead-magnoniobate-based solid solutions. *Phys. Solid State* **45**, 1305–1309 (2003).
32. Pandya, S. et al. Direct measurement of pyroelectric and electrocaloric effects in thin films. *Phys. Rev. Appl.* **7**, 034025 (2017).
33. Maria, J.-P., Hackenberger, W. & Trolier-McKinstry, S. Phase development and electrical property analysis of pulsed laser deposited $Pb(Mg_{1/3}Nb_{2/3})O_3$–$PbTiO_3$ (70/30) epitaxial thin films. *J. Appl. Phys.* **84**, 5147–5154 (1998).
34. Colla, E. V., Yushin, N. K. & Viehland, D. Dielectric properties of $(PMN)_{(1-x)}(PT)_x$ single crystals for various electrical and thermal histories. *J. Appl. Phys.* **83**, 3298–3304 (1998).
35. Ang, C. & Yu, Z. Dc electric-field dependence of the dielectric constant in polar dielectrics: multipolarization mechanism model. *Phys. Rev. B* **69**, 174109 (2004).
36. Li, Z., Xu, Z., Yao, X. & Cheng, Z. Y. Phase transition and phase stability in [110]-, [001]-, and [111]-oriented $0.68Pb(Mg_{1/3}Nb_{2/3})O_3$–$0.32PbTiO_3$ single crystal under electric field. *J. Appl. Phys.* **104**, 024112 (2008).
37. Bai, F. et al. X-ray and neutron diffraction investigations of the structural phase transformation sequence under electric field in $0.7Pb(Mg_{1/3}Nb_{2/3})$–$0.3PbTiO_3$ crystal. *J. Appl. Phys.* **96**, 1620–1627 (2004).
38. Xu, G., Zhong, Z., Bing, Y., Ye, Z.-G. & Shirane, G. Electric-field-induced redistribution of polar nano-regions in a relaxor ferroelectric. *Nat. Mater.* **5**, 134–140 (2006).
39. Takenaka, H., Grinberg, I., Liu, S. & Rappe, A. M. Slush-like polar structures in single-crystal relaxors. *Nature* **546**, 391–395 (2017).
40. Olsen, R. B. & Brown, D. D. High efficiency direct conversion of heat to electrical energy-related pyroelectric measurements. *Ferroelectrics* **40**, 17–27 (1982).
41. McKinley, I. M., Lee, F. Y. & Pilon, L. A novel thermomechanical energy conversion cycle. *Appl. Energy* **126**, 78–89 (2014).
42. Uršič, H. et al. Specific heat capacity and thermal conductivity of the electrocaloric $(1-x)Pb(Mg_{1/3}Nb_{2/3}O_3$–$xPbTiO_3$ ceramics between room temperature and 300 °C. *J. Microelectron. Electron. C* **45**, 260–265 (2015).
43. Novak, N., Cordoyiannis, G. & Kutnjak, Z. Dielectric and heat capacity study of $(Pb(Mg_{1/3}Nb_{2/3})O_3)_{0.74}$–$(PbTiO_3)_{0.26}$ ferroelectric relaxor near the cubic–tetragonal–rhombohedral triple point. *Ferroelectrics* **428**, 43–48 (2012).
44. Zhu, H., Pruvost, S., Guyomar, D. & Khodayari, A. Thermal energy harvesting from $Pb(Zn_{1/3}Nb_{2/3})_{0.955}Ti_{0.045}O_3$ single crystals phase transitions. *J. Appl. Phys.* **106**, 124102 (2009).
45. Khodayari, A., Pruvost, S., Sebald, G., Guyomar, D. & Mohammadi, S. Nonlinear pyroelectric energy harvesting from relaxor single crystals. *IEEE Trans. Ultrason. Ferroelectr. Freq. Control* **56**, 693–698 (2009).
46. Kandilian, R., Navid, A. & Pilon, L. The pyroelectric energy harvesting capabilities of PMN–PT near the morphotropic phase boundary. *Smart Mater. Struct.* **20**, 055020 (2011).
47. Lee, F. Y., Navid, A. & Pilon, L. Pyroelectric waste heat energy harvesting using heat conduction. *Appl. Therm. Eng.* **37**, 30–37 (2012).
48. Nguyen, H., Navid, A. & Pilon, L. Pyroelectric energy converter using co-polymer P(VDF-TrFE) and Olsen cycle for waste heat energy harvesting. *Appl. Therm. Eng.* **30**, 2127–2137 (2010).
49. Cha, G. & Ju, Y. S. Pyroelectric energy harvesting using liquid-based switchable thermal interfaces. *Sens. Actuat. A* **189**, 100–107 (2013).

Acknowledgements

S.P. acknowledges support from the Army Research Office under grant W911NF-14-1-0104. J.W. acknowledges support from a UC Berkeley Graduate Fellowship. J.K. acknowledges support from the US Department of Energy, Office of Science, Office of Basic Energy Sciences through grant no. DE-SC-0012375 for development of the relaxor materials. R.G. acknowledges support from the National Science Foundation under grant OISE-1545907. A.D. acknowledges support from the National Science Foundation under grant DMR-1708615. L.W.M. acknowledges support of the US Department of Energy, Office of Science, Office of Basic Energy Sciences, Materials Sciences and Engineering Division under contract no. DE-AC02-05-CH11231: Materials Project programme KC23MP for development of advanced functional materials.

Author contributions

S.P. and L.W.M. conceived the central concepts and designed the experiments. J.K. synthesized the materials. S.P. completed the electrical studies. J.K. and R.G. completed the structural characterization of the materials. S.P. and J.W. completed the thermal characterization and implemented the energy conversion cycles. S.P. conducted additional thermal–electrical studies that contributed to the understanding of the data. J.W. and C.D. contributed to the development of both the analytical and finite-element-based heat transport models. J.W., J.K. and A.D. contributed to analysis, discussions and understanding of the data and the development of the manuscript. S.P. and L.W.M. wrote the core of the manuscript. All authors discussed the results and implications of the work and commented on the manuscript at all stages.

Competing interests

The authors declare no competing interests.

Additional information

Supplementary information is available for this paper at https://doi.org/10.1038/s41563-018-0059-8.

Reprints and permissions information is available at www.nature.com/reprints.

Correspondence and requests for materials should be addressed to L.W.M.

Publisher's note: Springer Nature remains neutral with regard to jurisdictional claims in published maps and institutional affiliations.

Methods

Thin-film growth. This work focuses on 150 nm 0.68Pb($Mg_{1/3}Nb_{2/3}$)O_3–0.32$PbTiO_3$ (PMN–PT)/20 nm $Ba_{0.5}Sr_{0.5}RuO_3$ heterostructures grown on (110)-oriented, single-crystalline $NdScO_3$ substrates by pulsed-laser deposition using a KrF excimer laser (248 nm, LPX 300, Coherent), in an on-axis geometry with a 60 mm target-to-substrate spacing. PMN–PT growth was carried out at a deposition temperature of 600 °C in a dynamic oxygen pressure of 200 mtorr using a laser fluence of 1.8 J cm^{-2} and a laser repetition rate of 2 Hz. The $Ba_{0.5}Sr_{0.5}RuO_3$ bottom electrode layer was grown at a temperature of 750 °C in a dynamic oxygen pressure of 20 mtorr by ablating a $Ba_{0.5}Sr_{0.5}RuO_3$ target (Praxair) at a laser fluence of 1.85 J cm^{-2} and a laser repetition rate of 3 Hz. Following growth, the heterostructures were cooled to room temperature in a static oxygen pressure of 760 torr at 10 °C min^{-1}.

Device fabrication. Following the growth of 150 nm 0.68Pb($Mg_{1/3}Nb_{2/3}$)O_3–0.32$PbTiO_3$ (PMN–PT)/20 nm $Ba_{0.5}Sr_{0.5}RuO_3$/$NdScO_3$ (110) substrates, the electrothermal characterization devices are produced via a multistep, microfabrication process, according to ref. [32], some of which is reproduced here for completeness. Briefly, the relaxor–ferroelectric heterostructure is lithographically patterned and ion-milled to define the bottom electrode and the relaxor–ferroelectric 'active' layer (Fig. 1a of ref. [32]). After this step, the bottom electrode ($Ba_{0.5}Sr_{0.5}RuO_3$) is removed from everywhere except under the active layer and the bottom electrode probe pad. To define the top electrode, 90 nm $SrRuO_3$ is selectively deposited using an inverse MgO hard-mask process. This establishes a rectangular ferroelectric capacitor geometry (300 μm × 20 μm). The $SrRuO_3$ deposited over the active-layer mesa does not contact the $SrRuO_3$ deposited on the ion-milled region of the substrate, but a small gap is left in between. This is done purposefully to ensure that deposition on the sidewall of the ferroelectric layer does not electrically short to the bottom electrode. Next, a 200-nm-thick blanket layer of SiN_x is deposited on the symmetric ferroelectric capacitor structure using plasma-enhanced chemical vapour deposition ($SiH_4 + NH_3$ based) at 350 °C. This nitride layer is selectively patterned and etched using reactive ion etching in a SF_6 plasma, resulting in an electrically insulating film on top of the ferroelectric capacitor. Finally, a 100-nm-thick platinum thin-film resistance heater is sputtered in the shape of a thin strip with four probe pads (two outer and two inner pads; see the geometry in Fig. 1a of ref. [32]) to define the thermal circuit (Fig. 1b of ref. [32]). The top and the bottom electrode contact pads are also defined in this step. The top electrode platinum contact pad runs over the SiN_x and contacts the top $SrRuO_3$ (see the highlighted region in Fig. 1b of ref. [32]) while the bottom electrode platinum contact connects to the bottom $Ba_{0.5}Sr_{0.5}RuO_3$ after the device gets wire bonded.

Structural characterization. Wide-angle θ–2θ X-ray diffraction patterns (Supplementary Fig. 1a) and asymmetric reciprocal space maps (Supplementary Fig. 1b) were obtained with a Panalytical X'Pert Pro X-ray Diffraction machine with a Cu source.

Electrical characterization. Ferroelectric and dielectric properties were measured for six devices on the heterostructure. Polarization–electric field hysteresis loops were measured using a Precision Multiferroic Tester (Radiant Technologies) (Fig. 1b) that uses a virtual-ground method to measure ferroelectric hysteresis loops. Temperature- and electric-field-dependent low-field permittivity was measured using an E4990A Impedance Analyzer (Agilent Technologies) using an a.c. excitation voltage of 10 mV at various frequencies (Supplementary Fig. 2a). Burns temperature, below which short-range-ordered polar nano-regions begin to form, is calculated by measuring the deviation from the Curie–Weiss behaviour (Supplementary Fig. 2b).

Pyroelectric measurements. Average heater temperature amplitude (3ω measurement). Current supplied to the metal heater line (using a Keithley 6221 a.c. current source) results in power dissipation (Joule heating) as $P = I^2R$. Thus, a sinusoidal input current, $I = I_0\cos(\omega t)$, results in power dissipation at d.c. and 2ω and, therefore, a temperature rise of the line also at d.c. and 2ω,

$$\theta = \theta_{\mathrm{d.c.}} + \theta_0\cos(2\omega t + \phi) \tag{1}$$

where $\theta_{\mathrm{d.c.}}$ is the d.c. temperature rise, θ_0 is the a.c. temperature amplitude and φ indicates a phase lag that is determined by geometry and material properties. The oscillating temperature causes the resistance of the line to vary as $R = R_0(1 + \alpha\theta)$, where α is the temperature coefficient of resistance. Finally, when mixed with the input current, the resulting voltage drop across the line is, according to Ohm's law,

$$\begin{aligned} V(\omega) &= R_0 I_0 \cos(\omega t)\,[1 + \alpha\theta_{\mathrm{d.c.}}] \\ &+ \frac{R_0 I_0}{2}\alpha\theta_0\cos(\omega t + \phi) + \frac{R_0 I_0}{2}\alpha\theta_0\cos(3\omega t + \phi) \end{aligned} \tag{2}$$

Using an SRS SR830 lock-in amplifier, we measure the third harmonic of the voltage signal and thus determine the average heater temperature amplitude as[50]

$$\theta_0 = 2\frac{V_{3\omega}}{R_0 I_0 \alpha} = 2\frac{\mathrm{d}T}{\mathrm{d}R}\frac{V_{3\omega}}{I_0} \tag{3}$$

where $V_{3\omega}$ is the amplitude of the third-harmonic voltage.

Temperature coefficient of resistance (TCR or α). The temperature coefficient of resistance (TCR), $\alpha = \frac{\mathrm{d}R}{\mathrm{d}T}\frac{1}{R_0}$, where R_0 is the zero-current resistance at some reference temperature, is the driving force behind the resistance thermometry used to determine the average temperature of the heater line. This TCR must be calibrated for each device since it is dependent on the deposition parameters and can also vary significantly from bulk values, leading to variations by up to a factor of ~2 from handbook values in practice.

The sample is first heated to a desired temperature using a heating stage with a thermal mass much larger than the sample. Then the voltage is measured for a series of increasing current inputs and the resistance at each current is determined via Ohm's law. The resulting data are plotted as $R = \frac{V}{I}$ as a function of power $P = IV$, and a linear fit is used to determine R_0 from the zero-power limit (that is, the y intercept) for the given temperature. This process is then repeated for several more temperatures over a predetermined range (~10 K here). Finally, the resulting $R_0(T)$ is plotted against temperature and a linear fit is used to determine R_0 at 0 °C and $\frac{\mathrm{d}R}{\mathrm{d}T}$, the slope of the line. The TCR is then calculated as $\alpha = \frac{\mathrm{d}R}{\mathrm{d}T}\frac{1}{R_0}$.

Average ferroelectric temperature amplitude (validity of one-dimensional approximation). To be rigorous in the estimate of π, we also account for lateral heat spreading in the films since the effective area of the relaxor ferroelectric heated via the oscillating temperature on the top heater line with area $2b_{\mathrm{heater}}L$ is not necessarily the same as the electrode area $2b_{\mathrm{electrode}}L$ used to collect the pyroelectric current (Supplementary Fig. 8a). Therefore, an effective current-collecting area is defined as $2b_{\mathrm{eff}}L$, where b_{eff} is the effective half-width of the heater line. A numerical finite element analysis (FEA) package was employed to evaluate the appropriate geometric correction to π (Supplementary Fig. 8b).

The temperature amplitude of the ferroelectric film does not vary by more than a few per cent through the ferroelectric film's thickness (the z direction of Supplementary Fig. 8a) but the temperature profile does vary significantly along the x direction. For a one-dimensional non-uniform profile such as this, the total measured pyrocurrent is rigorously defined as

$$i_{\mathrm{p}} = \pi A\frac{\mathrm{d}T}{\mathrm{d}t} = \pi L 2\omega\left(2\int_0^{b_{\mathrm{eletrode}}}\theta(x)\,\mathrm{d}x\right) \tag{6}$$

where $\theta(x)$ is the temperature amplitude of the ferroelectric response at the z plane halfway through the film thickness, the time derivative of the temperature amplitude (corrected for the phase lag) has been taken explicitly giving a factor of 2ω, and the extra factor of 2 arises because the integral accounts for only half of the electrode width. The measured temperature amplitude used to determine π is θ_{FE}. Note that θ_{FE} is determined from θ_{heater} and is therefore an estimate of the average temperature amplitude of the ferroelectric only out to b_{heater}, whereas i_{p} is collected via the electrode with a larger half-width ($b_{\mathrm{electrode}} > b_{\mathrm{heater}}$) necessitating a correction.

The goal of using FEA is to determine an effective half-width, b_{eff}, that properly combines the disparate $b_{\mathrm{electrode}}$ and b_{heater} in such a way as to return the rigorous definition of the pyrocurrent, i_{p}. Mathematically, this requirement corresponds to

$$\pi L 2\omega 2b_{\mathrm{eff}}\theta_{\mathrm{FE}} = \pi L 2\omega\left(2\int_0^{b_{\mathrm{electrode}}}\theta(x)\,\mathrm{d}x\right) \tag{7}$$

$$b_{\mathrm{eff}} = \frac{\int_0^{b_{\mathrm{electrode}}}\theta(x)\,\mathrm{d}x}{\theta_{\mathrm{FE}}} \tag{8}$$

As θ_{FE} is

$$\theta_{\mathrm{FE}} = \frac{1}{b}\int_0^{b_{\mathrm{heater}}}\theta(x)\,\mathrm{d}x \tag{9}$$

we have found the result sought

$$b_{\mathrm{eff}} = b_{\mathrm{heater}}\frac{\int_0^{b_{\mathrm{electrode}}}\theta(x)\,\mathrm{d}x}{\int_0^{b_{\mathrm{heater}}}\theta(x)\,\mathrm{d}x} \tag{10}$$

The above equation shows that b_{eff} is simply the heater half-width, b_{heater}, multiplied by the ratio of two integrals. Appropriately employing FEA can give $\theta(x)$ at any height in the stack and can therefore be used to solve for the numerical factor (the ratio of the two integrals) in b_{eff}.

Using a commercial FEA package, COMSOL Multiphysics, the two-dimensional time-periodic heat diffusion problem is solved and the temperature amplitude $\theta(x,z)$ with appropriate boundary conditions (that is, uniform periodic heat flux from the heater and adiabatic boundaries elsewhere) is used to evaluate the integrals. The FEA solution was verified against the analytical solution for the average heater temperature amplitude, θ_{heater} (ref. [50]). The magnitudes of the

integrals in equation (10) are found and their ratio determined for the given system with properties specified in Supplementary Table 1 and for many frequencies, as can be seen in Supplementary Fig. 9.

Measurement of pyroelectric current, i_p. With the measured average temperature oscillation in the ferroelectric, measurement of i_p permits the extraction of π. As described in ref. [32], the current i_{total} is measured via the bottom electrode using a lock-in amplifier (Stanford Research, SR830) (Fig. 1a). The top electrode is deliberately held at ground potential to shield capacitive coupling between the thermal and ferroelectric measurement circuits. i_p is extracted from i_{total} by taking the component of i_{total} that leads the temperature change by 90°. Ultimately, π is calculated as $\pi = i_p\left(A\frac{dT}{dt}\right)^{-1}$, where A is the area equal to $2b_{eff}L$.

Pyroelectric Ericsson cycle. The ideal pyroelectric Ericsson cycle begins with an isothermal (T_{low}) change of electric field ($E_{low} \rightarrow E_{high}$; $1 \rightarrow 2$, Fig. 3a) that polarizes the system. This is followed by an isoelectric (E_{high}) absorption of heat ($T_{low} \rightarrow T_{high}$; $2 \rightarrow 3$, Fig. 3a). Next, the electric field is isothermally (T_{high}) reduced ($E_{high} \rightarrow E_{low}$; $3 \rightarrow 4$, Fig. 3a). Finally, the heat is expelled isoelectrically (E_{low}) ($T_{high} \rightarrow T_{low}$; $4 \rightarrow 1$, Fig. 3a). In our solid-state device, this is implemented by applying a carefully chosen time-dependent temperature and applied electric field across the relaxor ferroelectric. By applying a sinusoidally varying current $i_h(t)$ at 1ω (red curve, Fig. 3b) that locally heats the heterostructure via Joule heating, the temperature of the heterostructure is sinusoidally varied with a variable amplitude at a desired frequency 2ω (blue curve, Fig. 3b). A synchronized periodic electric field $E(t)$ is applied across the heterostructure in a nearly square-wave fashion (Fig. 3c). The heating current and the electric field are offset by a phase ϕ to account for the thermal phase lag using the measured phase lag from the 3ω method (Supplementary Fig. 3). In our device, isothermal polarization and depolarization is achieved by switching the electric field exactly where the temperature achieves its extrema. In other words, the electric field changes from high to low or vice versa while the temperature goes through a maximum or a minimum with less than 5% change in the temperature. This small but finite 5% temperature-change window was chosen so as not to change the electric field using a step function that results in a very large capacitive current saturating our current-to-voltage amplifier. The total current in response to this periodically varying temperature and electric field is measured using a variable-gain low-noise current amplifier (DLPCA-200, Femto). All three signals (heating current, electric field and measured total current) are measured using a digital oscilloscope (InfiniiVision DSO-X-4024A, Agilent Technologies). The measured total current can then be numerically integrated to calculate the change in polarization, $\Delta P(t)$. However, it should be noted that the electrode area for collecting the dielectric current ($A_{electrode}$) is larger than the area getting heated or the effective area for collecting the pyroelectric current (A_{heater}); therefore, the net change in polarization is calculated by separately integrating the current using the respective areas as

$$\Delta P(t) = \frac{1}{A_{heater}}\int_0^t i_p(t)\,dt + \frac{1}{A_{electrode}}\int_0^t i_d(t)\,dt \quad (13)$$

To separate the current contribution from the change in capacitance (dielectric current $i_d(t)$) versus the pyroelectric current ($i_p(t)$), the heating is turned off ($i_h(t) = 0$) to measure just the dielectric current alone. Since the dielectric current does not change dramatically as a function of temperature under large applied field (due to quenched dielectric permittivity), this dielectric current is subtracted from the total measured current to get the pyroelectric current. Using equation (13), $\Delta P(t)$ is calculated and further plotting $\Delta P(t)$ versus $E(t)$ gives the pyroelectric Ericsson cycle with the cyclic loop (Fig. 3e).

Work done per cycle per volume (equivalently energy density per cycle) was calculated by numerically extracting the area of the loop ($\oint E \,.\, dP$). Scaled efficiency (% of Carnot) of the cycle was calculated as

$$\eta = \frac{T_{high}}{\Delta T}\frac{\sum W}{Q_{in}} = \frac{T_{high}}{\Delta T}\frac{\oint E \,.\, dP}{\int_{T_{low}}^{T_{high}} C(T)\,dT} \quad (14)$$

where $\left(\frac{T_{high}}{\Delta T}\right)^{-1}$ is the Carnot efficiency and $C(T)$ is the temperature-dependent volumetric heat capacity of the ferroelectric film. In our calculations, $C(T)$ is extracted by fitting the experimental data from ref. [41].

Data availability. The data that support the findings of this study are available from the corresponding author upon reasonable request.

References

50. Cahill, D. G. Thermal conductivity measurement from 30 to 750 K: the 3ω method. *Rev. Sci. Instrum.* **61**, 802 (1990).